Chemical Science

ROYAL SOCIETY OF CHEMISTRY

EDGE ARTICLE

View Article Online
View Journal | View Issue

Cite this: *Chem. Sci.*, 2021, **12**, 14473

All publication charges for this article have been paid for by the Royal Society of Chemistry

Aptamer-modified DNA tetrahedra-gated metal–organic framework nanoparticle carriers for enhanced chemotherapy or photodynamic therapy†

Pu Zhang,‡[a] Amit Fischer,‡[a] Yu Ouyang,[a] Jianbang Wang,[a] Yang Sung Sohn,[b] Rachel Nechushtai,[b] Eli Pikarsky,[c] Chunhai Fan [d] and Itamar Willner *[a]

UiO-66 metal–organic framework nanoparticles (NMOFs) gated by aptamer-functionalized DNA tetrahedra provide superior biomarker-responsive hybrid nano-carriers for biomedical applications. Hybrid nano-carriers consisting of ATP-aptamer or VEGF-aptamer functionalized tetrahedra-gated NMOFs are loaded with the chemotherapeutic drug, doxorubicin (DOX). In the presence of ATP or VEGF, both abundant in cancer cells, the tetrahedra-gated NMOFs are unlocked to release the drug. Enhanced and selective permeation of the DOX-loaded ATP/VEGF-responsive tetrahedra-gated NMOFs into MDA-MB-231 breast cancer cells as compared to the reference ATP/VEGF-responsive duplex-gated NMOFs or non-malignant MCF-10A epithelial breast cells is observed. This results in enhanced and selective cytotoxicity of the tetrahedra-gated DOX-loaded NMOFs toward the malignant cells. Additional nano-carriers, consisting of photosensitizer Zn(II) protoporphyrin IX (Zn(II)-PPIX)-loaded VEGF-responsive tetrahedra-gated NMOFs, are introduced. The VEGF-triggered unlocking of the NMOFs yields separated G-quadruplex-VEGF aptamer complexes conjugated to the tetrahedra, resulting in the release of loaded Zn(II)-PPIX. Association of the released Zn(II)-PPIX to the G-quadruplex structures generates highly fluorescent supramolecular Zn(II)-PPIX/G-quadruplex VEGF aptamer-tetrahedra structures. The efficient and selective generation of the highly fluorescent Zn(II)-PPIX/G-quadruplex VEGF aptamer-tetrahedra nanostructures in malignant cells allows the light-induced photosensitized generation of reactive oxygen species (ROS), leading to high-efficacy PDT treatment of the malignant cells.

Received 2nd August 2021
Accepted 12th October 2021

DOI: 10.1039/d1sc04229g

rsc.li/chemical-science

Introduction

Sense-and-treat systems in which stimuli-responsive drug carriers respond to a disease biomarker attract growing interest as autonomous, self-sustained, therapeutic means for personalized medicine.[1] For example, the development of glucose-responsive insulin-carriers represents a major challenge in the area of sense-and-treat systems[2] and different glucose responsive insulin-loaded carriers were reported as potential sense-and-treat systems of diabetes, such as polymers,[3] microcapsules[4] or nanoparticles.[5] Also, microRNA-responsive drug carriers[6] or aptamer-functionalized drug-loaded nanoparticles responding to protein biomarkers[7] were suggested as versatile self-sustained sense-and-treat systems of cancer or macular diseases. Vascular endothelial growth factor (VEGF) is a key regulator of pathologic and physiologic angiogenesis[8] and is considered as an important signaling protein biomarker, for different diseases, such as cancer,[9] rheumatoid arthritis,[10] proliferating retinopathy,[11] psoriasis,[12] and Parkinson's disease.[13] Different sensing platforms for sensing VEGF were reported including antibody-based optical assays,[14] aptamer-based electrochemical methods[15] or optical sensing assays based on semiconductor quantum dots.[16] Additionally, functional DNA nanostructures were used for the optical detection of VEGF.[17]

Metal–organic framework nanoparticles (NMOFs) are crystalline materials composed of metal-ions crosslinked by organic ligands.[18] Different applications of NMOFs were reported, including their use as sensors,[19] membrane separation materials,[20] optoelectronic devices[21] and biological probes.[22] The

[a]*Institute of Chemistry, Center for Nanoscience and Nanotechnology, The Hebrew University of Jerusalem, Jerusalem 91904, Israel. E-mail: itamar.willner@mail.huji.ac.il*

[b]*Institute of Life Science, The Hebrew University of Jerusalem, Jerusalem 91904, Israel*

[c]*The Lautenberg Center for Immunology and Cancer Research, The Hebrew University of Jerusalem, Jerusalem 91904, Israel*

[d]*School of Chemistry and Chemical Engineering, Frontiers Science Center for Transformative Molecules, National Center for Translational Medicine, Shanghai Jiao Tong University, Shanghai, 200240, China*

† Electronic supplementary information (ESI) available. See DOI: 10.1039/d1sc04229g

‡ These authors contributed equally to this work.

biocompatibility of NMOFs enables their use as drug carriers and controlled release systems.[23] Specifically, the functionalization of NMOFs with stimuli-responsive gating units was utilized to develop signal controlled drug delivery systems for biomedical applications.[24] Different triggers, such as pH,[25] redox signals[26] or ions[27] were applied to unlock the drug-loaded NMOFs and to release the entrapped drugs. One important subclass of gated drug-loaded NMOFs includes stimuli-responsive nucleic acid-locked drug-loaded NMOFs, gaining from the remarkable versatility of nucleic acid sequences to generate recognition elements as well as structural elements. Different triggers to unlock nucleic acid-gated drug-loaded NMOFs were reported, including pH,[28] enzymes and DNAzymes,[29] and biomarker-responsive gates triggered by miRNAs,[30] VEGF or ATP.[31] Targeting of the drug-loaded NMOFs to cells using aptamers and their cytotoxicity towards different cancer cells have been demonstrated.

Recently, all-DNA tetrahedra nanostructures are attracting intense research efforts.[32] The unique features of DNA tetrahedra include their structural rigidity, tunable sizes, and the ability to engineer specific sequences into the edges of the tetrahedra structures or the anchoring of sequence-specific tethers to their corners of the tetrahedra structures.[33] These unique properties of DNA tetrahedra were applied for sensing,[34] logic gate operations,[35] design of dynamic networks[36] and their use as functional scaffolds for the fabrication of chiral building blocks and chiroplasmonic nanostructures.[37] The biomedical applications of DNA tetrahedra are particularly intriguing. Effective cell permeation of the tetrahedra nanostructures, attributed to the sharp tetrahedra corners, was demonstrated,[38] and by the functionalization with ligands or drugs, targeted drug delivery with the DNA tetrahedra was achieved.[39] In addition, intracellular sensing[40] and imaging[41] using DNA tetrahedra were reported. We hypothesized that DNA tetrahedra, that are linked to the NMOFs *via* a stimuli-responsive nucleic acid tether, could increase the functionality of our sense-and-treat trigger gated nanoparticles.

In the present study, we introduce aptamer-modified DNA tetrahedra-functionalized NMOFs as carriers for chemotherapy or photodynamic therapy. Here we tested different loads including a fluorescent dye, the chemotherapeutic drug doxorubicin, DOX, or Zn(II) protoporphyrin IX (Zn(II)-PPIX) as a fluorophore and photodynamic therapy agent. The NMOFs carriers, caged by the aptamer-functionalized tetrahedra gates, are unlocked by ATP or VEGF which are abundant in cancer cells, leading to the selective release of the loads in cancer cells. The systems introduce an autonomous sense-and-treat path of cancer cells and demonstrate effective permeation of the DNA tetrahedra-gated NMOFs into cancer cells, leading to selective cytotoxic and photodynamic treatment of MDA-MB-231 breast cancer cells. The systems introduce a DNA tetrahedra-enhanced autonomous sense-and-treat path of cancer cells.

Results and discussion, experimental

The synthesis of ATP-responsive UiO-66 NMOFs loaded with a dye (Rhodamine 6G, Rh 6G) or doxorubicin (DOX) and gated by the ATP aptamer-functionalized DNA tetrahedra, and the ATP-stimulated unlocking of the NMOFs are schematically presented in Fig. 1. Azide-modified terephthalic acid was reacted with $ZrOCl_2$ to yield the azide-modified UiO-66 NMOFs. The amido nucleic acid (**1**)-modified DBCO (DBCO = dibenzocyclooctyne) was covalently linked to the NMOFs using the click chemistry principles, to yield the (**1**)-modified NMOFs, Fig. 1(A). The (**1**)-functionalized NMOFs were loaded with Rh 6G or DOX and subsequently locked by the ATP aptamer-functionalized DNA tetrahedra, where the tether (**1′**) associated with the tetrahedra includes the ATP-aptamer sequence, complementary to the nucleic acid units (**1**), linked to the NMOFs. The (**1**)/(**1′**)-bridged hybridization of the tetrahedra to the NMOFs yields the ATP-responsive tetrahedra gating units. It should be noted that the gating of the drug-loaded NMOFs is performed in two steps, where DOX is loaded into the NMOFs that are subsequently gated by the hybridization of the tetrahedra units. Separate

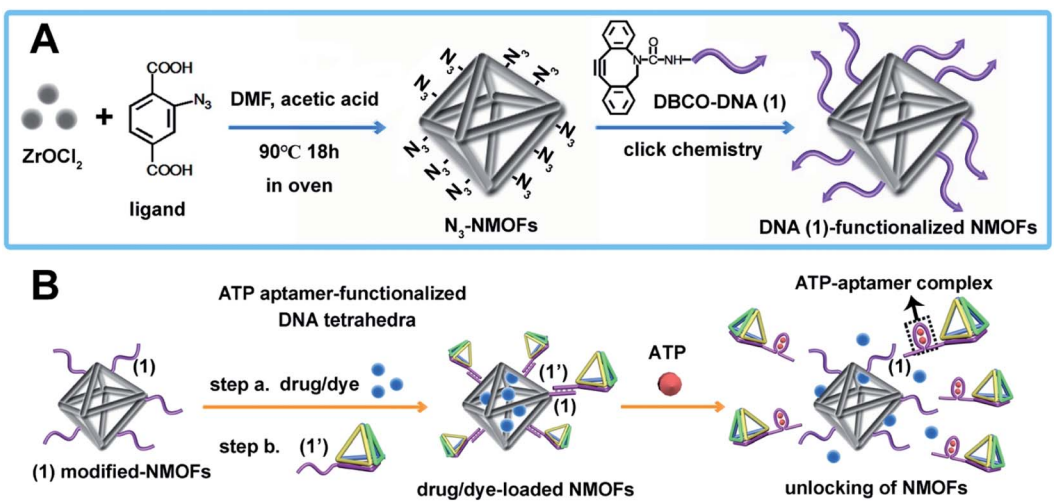

Fig. 1 (A) Schematic synthesis of the nucleic acid-tethered UiO-66 NMOFs. (B) Schematic loading and gating of the nucleic acid-modified UiO-66 NMOFs with ATP aptamer-functionalized DNA tetrahedra gates. The gated NMOFs are unlocked by ATP.

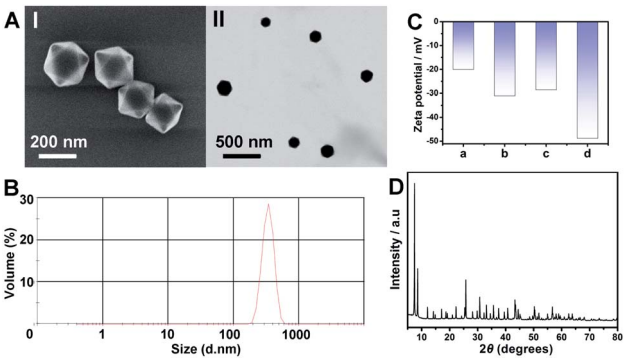

Fig. 2 (A) SEM image (panel I) and STEM image (panel II) of the (**1**)-modified UiO-66 NMOFs. (B) Dynamic light scattering spectrum of the (**1**)-modified UiO-66 NMOFs. (C) Zeta potential values of (a) The bare N_3-modified UiO-66 NMOFs, (b) The (**1**)-modified UiO-66 NMOFs, (c) The DOX-loaded (**1**)-modified UiO-66 NMOFs, and (d) The tetrahedra-gated DOX-loaded UiO-66 NMOFs. (D) The XRD spectrum of the (**1**)-modified UiO-66 NMOFs.

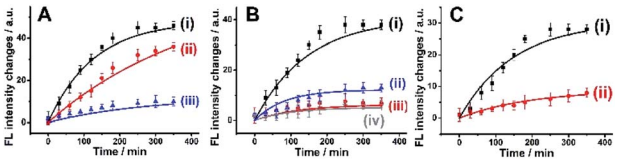

Fig. 3 (A) Time-dependent release of Rh 6G from the ATP-responsive tetrahedra-gated NMOFs in the presence of (i) 25 mM ATP; (ii) 10 mM ATP and (iii) 0 mM ATP. (B) Time-dependent release of Rh 6G from the ATP-responsive tetrahedra-gated NMOFs in the presence of (i) 25 mM ATP; (ii) 25 mM GTP; (iii) 25 mM CTP and (iv) 25 mM TTP. (C) Time-dependent release of DOX from the ATP-responsive tetrahedra-gated NMOFs: (i) in the presence of ATP, 25 mM. (ii) In the absence of ATP. Error bars derived from $N = 3$ experiments.

experiment indicated that no leakage of DOX from the tetrahedra took place. The mechanism of unlocking of the ATP-responsive tetrahedra-gated NMOFs and the release of the loads is schematically presented in Fig. 1(B). In the presence of ATP, the formation of the ATP-aptamer complexes displaces the tetrahedra locks, resulting in the dissociation of tetrahedra from NMOFs and the release of the loads. The assembly of the intact DNA tetrahedra nanostructures was confirmed by electrophoretic separation and by complementary atomic force microscopy (AFM) measurements that revealed an average tetrahedra height of 0.9 nm and width of 10 nm, Fig. S1.† The (**1**)-modified NMOFs were further characterized by SEM and STEM imaging showing a particle size distribution of 200–300 nm, Fig. 2(A), panel I and II, and dynamic light scattering measurements, displaying a size of *ca.* 400 nm, Fig. 2(B). The zeta potential of the (**1**)-modified NMOFs corresponded to *ca.* −30 mV and after loading with DOX and gating with the DNA tetrahedra to *ca.* −50 mV, Fig. 2(C), consistent with the increase negative charge of the DNA tetrahedra. It should be noted that the pore sizes of octahedral or tetrahedral UiO-66 NMOFs correspond to 11 Å and 8 Å,[42] respectively, and the size of DOX is *ca.* 13 Å × 10 Å, suggest that the drug accommodates partial volumes of the pores or, alternatively, accommodates inter pore domains of the porous structure. The X-ray diffraction (XRD) spectrum of the (**1**)-functionalized NMOFs, Fig. 2(D) is similar to the reported XRD spectrum of the base NMOFs, indicating that the crystalline structure of the NMOFs is retained after the surface modification of the particles. The surface coverage of the NMOFs by (**1**) was evaluated spectroscopically to be 27.3 nmols per mg of NMOFs, Fig. S2.† The loading of the NMOFs by Rh 6G or DOX corresponded to 65 or 68 nmols per mg of NMOFs, respectively (for details to evaluate the loading of Rh 6G/DOX see experimental details, Fig. S3, ESI†).

Fig. 3(A) depicts the time-dependent release of Rh 6G from ATP-responsive tetrahedra-gated NMOFs treated with two different concentrations of ATP, 25 mM, curve (i) and 10 mM, curve (ii). For comparison, the release of the dye in the absence of added ATP is shown in curve (iii). As is displayed, very low release of the Rh 6G is observed in the absence of added ATP. As the concentration of ATP increases, the release of the dye is faster consistent with the enhanced unlocking of the tetrahedra gates through the formation of the ATP-aptamer complexes. For the high concentration of ATP, the release profile reaches saturation after *ca.* 250 minutes implying the complete release of the load. Using an appropriate calibration curve that relates the fluorescence intensities of Rh 6G at variate concentrations, Fig. S3,† the saturated fluorescence intensity corresponds to a dye loading of 68 nmols per mg of NMOFs. This loading value agrees well with the spectroscopically evaluated loading upon preparation of the loaded gated NMOFs, Fig. S3.† The release of the loaded dye is selective to ATP, and subjecting the NMOFs to other nucleotide triphosphates, *i.e.*, GTP, TTP and CTP, results in only the residual release of the dye from NMOFs, Fig. 3(B). Fig. S4† shows the fluorescence spectra of the released Rh 6G at fixed time-intervals of 250 minutes after unlocking the NMOFs with different nucleotide triphosphates. This selectivity is consistent with the fact that the unlocking of the gates is specific to the formation of the ATP-aptamer complexes. Fig. 3(C) depicts the time-dependent release profile of the DOX load, in the presence of 25 mM ATP, curve (i). For comparison, the release profile of DOX from the drug-loaded NMOFs in the absence of ATP is shown in Fig. 3(C), curve (ii). From the saturated fluorescence value of released DOX (after 250 minutes), and using an appropriate calibration curve, the loading of DOX in the gated NMOFs was estimated to be 65 nmols per mg of NMOFs, a value similar to the spectroscopically-derived loading degree, see ESI, Fig. S3.† It should be noted that the minute time-dependent release of DOX, in the absence of ATP, Fig. 3(C), curve (ii), reaches a saturation level, after the time-interval of *ca.* 350 minutes. This release process is attributed to the escape of the load from imperfectly tetrahedra-locked sites. In addition, the loading capacity and unlocking by ATP of the tetrahedra-gated NMOFs were compared to a control system comprising of Rh 6G-loaded duplex-locked NMOFs, devoid of tetrahedra (The mechanism of unlocking of these duplex-gated NMOFs is shown in Fig. S5 (A)† and the time-dependent release profile of the Rh 6G is shown in Fig. S5(B)†). The comparison reveals that the tetrahedra-gated NMOFs have a similar loading capacity and a similar stimuli responsiveness curve to duplex-gated NMOFs.

Tetrahedra coated nanoparticles were reported to hold better cell permeation potential. Thus, the cell permeation efficiency and the cytotoxicity of the DOX-loaded ATP-responsive DNA tetrahedra-gated NMOFs carrier were examined. For this, a control system of DOX-loaded NMOFs gated by ATP aptamer-functionalized duplex (**1**)/(**1**″) units, Fig. 4(A), was prepared. The control NMOFs were prepared by loading the (**1**)-modified NMOFs with DOX and their subsequent gating with the nucleic acids strand (**1**″) that includes the ATP aptamer sequence, yet lacks the DNA tetrahedra component. The loading degree of the (**1**)/(**1**″)-gated NMOFs was 27.1 nmols per mg of NMOFs, see details, Fig. S6† and accompanying discussion. The coverage of the NMOFs gated by ATP aptamer-functionalized duplex units were very similar to the DNA tetrahedra-gated carriers. Thus, the (**1**)/(**1**″) duplex-gated DOX-loaded NMOFs provide an effective control system to probe the potential advantages of the DOX-loaded DNA tetrahedra-gated carriers. Two issues were addressed in the cellular experiments: (i) the cell permeation efficiency and cytotoxicity of DOX-loaded tetrahedra-gated NMOFs *vs.* DOX-loaded (**1**)/(**1**″) duplex-gated NMOF. (ii) The cell permeation efficiency and cytotoxicity of the DOX-loaded NMOFs towards MDA-MB-231 malignant cells, in comparison to non-malignant epithelial MCF-10A breast cells. Fig. 4(B), panel I shows representative confocal microscopy images of MDA-MB-231 cells treated with the DOX-loaded tetrahedra-gated NMOFs, whereas panel II shows the confocal images of MDA-MB-231 cells with the ATP-responsive duplex (**1**)/(**1**″)-gated DOX-loaded NMOFs. The fluorescence confocal microscopy images of MDA-MB-231 cells treated with DOX-loaded ATP-responsive DNA tetrahedra-gated NMOFs reveal significantly enhanced red fluorescence as compared to the fluorescence observed in the cells treated with the ATP-responsive (**1**)/(**1**″)-gated NMOFs, suggesting improved permeation of the tetrahedra-gated NMOFs into the cells. Fig. 4(B), panels III and IV show the confocal microscopy images of the MCF-10A cells treated with the DOX-loaded tetrahedra-gated NMOFs and the (**1**)/(**1**″)-gated NMOFs, respectively. Very weak fluorescence of

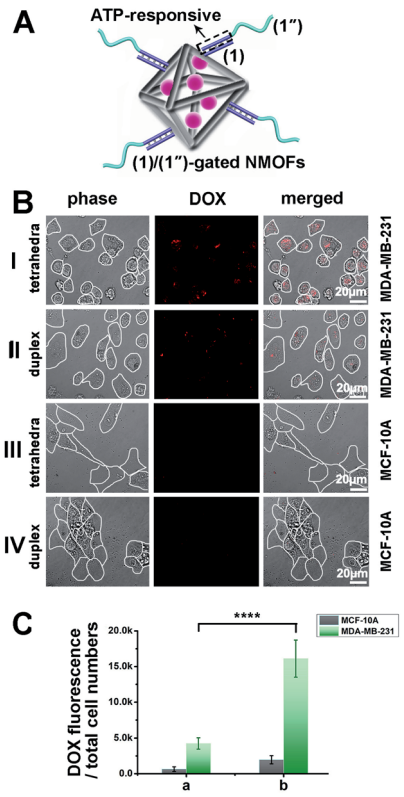

Fig. 4 Uptake of the DOX-loaded ATP-responsive tetrahedra-gated NMOFs by the MDA-MB-231 breast cancer cells and by MCF-10A epithelial breast cells, and the respective control uptake system consisting of the DOX-loaded ATP-responsive NMOFs gated by (**1**)/(**1**″) duplex locks probing the uptake by MDA-MB-231 cells or MCF-10A cells. (A) Schematic structure of the DOX-loaded gated by the ATP-responsive (**1**)/(**1**″) duplex locks. (B) Confocal microscopy images corresponding to: panel I-Uptake of the DOX-loaded ATP-responsive tetrahedra-gated NMOFs by MDA-MB-231 cells. Panel II-Uptake of the DOX-loaded ATP-responsive (**1**)/(**1**″) duplex-gated NMOFs by MDA-MB-231 cells. Panel III-Uptake of the DOX-loaded ATP-responsive tetrahedra-gated NMOFs by MCF-10A cells. Panel IV-Uptake of the DOX-loaded ATP-responsive (**1**)/(**1**″) duplex-gated NMOFs by MCF-10A cells. Cells treated with 60 μg mL^{-1} NMOFs for 6 hours. (C) Normalized integrated fluorescence intensities corresponding to the uptake of the DOX-loaded NMOFs (grey column for MCF-10A cells and green column for MDA-MB-231 cells) by (a) The control system composing of the DOX-loaded ATP-responsive (**1**)/(**1**″) duplex-gated NMOFs. (b) The DOX-loaded ATP-responsive tetrahedra-gated NMOFs. Uptake of the different NMOFs by cells is measured in more than 50 cells per field (±SD, from 10 fields). **** denotes P <0.0001 by t-test.

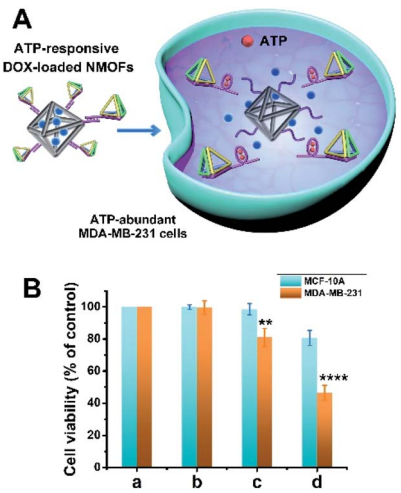

Fig. 5 (A) Schematic ATP-triggered unlocking of the gates and the release process of DOX proceed. (B) Cytotoxicity of the DOX-loaded ATP-responsive tetrahedra-gated NMOFs toward MDA-MB-231 cancer cells (orange) and MCF-10A control epithelial cells (blue) and comparison to the cytotoxicity of the DOX-loaded ATP-responsive (**1**)/(**1**″)-duplex gated NMOFs towards the respective cells: (a) untreated cells. (b) Cells treated with non-loaded NMOFs. (c) Cells treated with the DOX-loaded (**1**)/(**1**″)-duplex gated NMOFs. (d) Cells treated with the DOX-loaded tetrahedra-gated NMOFs. In all experiments, cells were treated with 60 μg mL^{-1} NMOFs for 6 hours and cell viability was evaluated after three days and the NMOFs included DOX-loading corresponding to 65 nmols per mg of NMOFs. Error bars derived from $N = 3$ experiments. ** denotes P <0.01, **** denotes P <0.0001 by t-test.

DOX is observed in these cells, indicating poor permeation of the gated NMOFs into the control MCF-10A epithelial cells. To quantitate these results, the normalized fluorescence intensities extracted from ten different frames of the respective cells treated with the tetrahedra-gated and (**1**)/(**1**″)-gated DOX-loaded NMOFs were derived, and the results are summarized in Fig. 4(C). The following significant conclusions are extracted: (i) the efficacy of cell permeation of the DOX-loaded tetrahedra-gated NMOFs or the (**1**)/(**1**″) duplex-gated NMOFs into the malignant MDA-MB-231 cancer cells is substantially higher as compared to the permeation of the respective NMOFs into the epithelial MCF-10A cells. (ii) The permeation of the DOX-loaded tetrahedra-gated NMOFs into the MDA-MB-231 cancer cells is *ca.* 3.5-fold higher as compared to the (**1**)/(**1**″)-gated NMOFs. Thus, the results suggest selectivity and enhanced cell permeation of the tetrahedra-gated carriers upon treatment of cancer cells.

Fig. 5 shows the cytotoxicity of the ATP-responsive tetrahedra-gated DOX-loaded NMOFs towards MDA-MB-231 cancer cells and the MCF-10A control epithelial cells, in comparison to the (**1**)/(**1**″) duplex-gated drug-loaded NMOFs. The cells were treated with 60 μg mL^{-1} NMOFs and cell viability was measured after three days. The ATP-induced release of DOX from the NMOFs, and the resulting cytotoxicity of the released drug towards the cancer cells are schematically presented in Fig. 5(A). For comparison, the cell viability of non-treated cells is shown in Fig. 5(B), panel (a). The result in panel (b) shows that the non-loaded tetrahedra-gated NMOFs have negligible effect on the viability of the MDA-MB-231 cells and MCF-10A cells (<2% cell death after three days of treatment). The MDA-MB-231 treated with the (**1**)/(**1**″)-duplex gated NMOFs, after this time interval, only 20% cell mortality and the MCF-10A *ca.* 2% motility were observed, respectively, panel (c). However, the MDA-MB-231 cells treated with DOX-loaded tetrahedra-gated NMOFs revealed 60% cell death while the normal cells showed less than 20% mortality, panel (d). The enhanced cytotoxicity and the selectivity of the tetrahedra-gated NMOFs are attributed to the superior permeation of the carriers into the cancer cells and to the over-expressed ATP-guided unlocking of the carriers in the cancer cells. The cytotoxicity of the DOX-loaded ATP-responsive tetrahedra-functionalized NMOFs is comparable, or slightly better, as compared to DOX-loaded ATP aptamer-responsive polymeric hydrogel particles.[43]

The superior delivery/permeation functions of stimuli-responsive drug-loaded DNA tetrahedra-functionalized NMOFs were broadened to include VEGF as trigger to unlock the gated NMOFs. VEGF, due to its angiogenic activities, is over-expressed in malignant cells, and thus could provide a versatile marker to release anti-cancer drugs or cancer cells treatment agents. Fig. 6(A) depicts the assembly and schematic functions of the VEGF-responsive DNA tetrahedra-functionalized dye/drug-loaded NMOFs. The NMOFs were functionalized with strand (**2**), using the click chemistry principle outlined in Fig. 1(A). The NMOFs were loaded with DOX or Rh 6G as drug model, and the loaded NMOFs were gated with DNA tetrahedra functionalized with the tether (**2**′). The tether (**2**′) includes the VEGF aptamer sequence. In the presence of VEGF, the tetrahedra gates are unlocked, through the formation of the VEGF-aptamer complexes, resulting in the release of the loads. Fig. 6(B) shows the VEGF-induced time-dependent release profile of Rh 6G at different concentrations of VEGF. As the concentration of VEGF increases, the release rate of Rh 6G is enhanced, and at a VEGF concentration corresponding to 2 μM, the release of the load reaches saturation after *ca.* 50 minutes. Using an

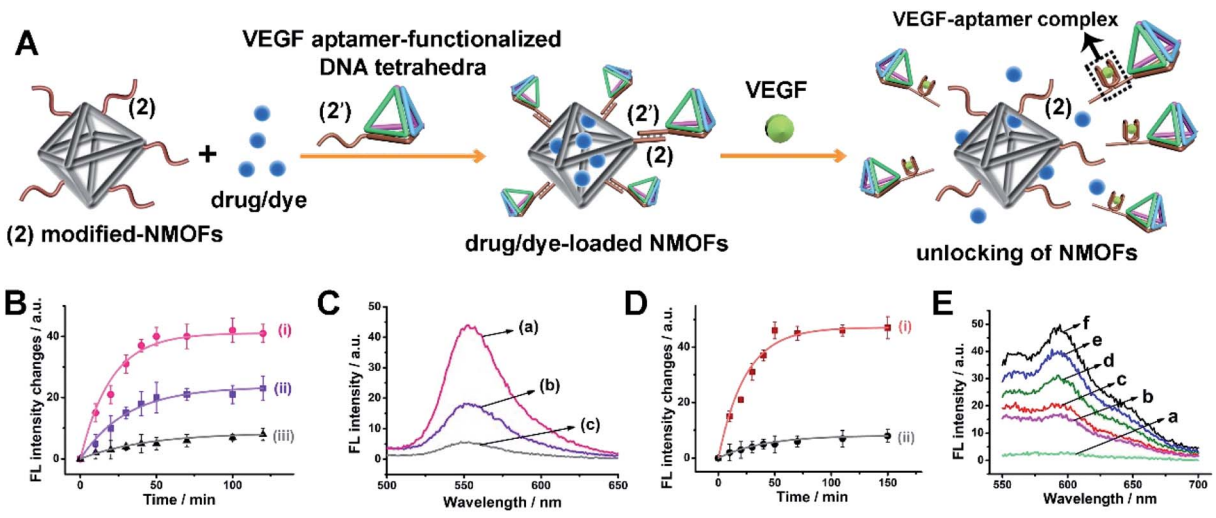

Fig. 6 (A) Schematic loading and gating of NMOFs with VEGF-responsive tetrahedra locks (loading = dye or DOX). (B) Time-dependent release of Rh 6G from the VEGF-responsive tetrahedra-gated NMOFs in the presence of (i) 2 μM VEGF; (ii) 1 μM VEGF; (iii) 0 μM VEGF. (C) Fluorescence spectra of Rh 6G released from VEGF-responsive tetrahedra-gated NMOFs in the presence of (a) 2 μM VEGF; (b) 1 μM VEGF; (c) 0 μM VEGF after a fixed time-interval of 50 minutes. (D) Time-dependent release of DOX from the VEGF-responsive tetrahedra-gated NMOFs in the presence of (i) 2 μM VEGF; (ii) 0 μM VEGF. (E) Fluorescence spectra of DOX released from VEGF-responsive tetrahedra-gated NMOFs in the presence of 2 μM VEGF at different time-intervals: (a) 0 minute; (b) 10 minutes; (c) 20 minutes; (d) 30 minutes; (e) 40 minutes; (f) 50 minutes. Error bars derived from $N = 3$ experiments.

appropriate calibration curve, the loading of the Rh 6G in the tetrahedra-gated NMOFs was derived, and it corresponded to 68 nmols per mg of NMOFs. Fig. 6(C) shows the fluorescence spectra of the released Rh 6G after unlocking the NMOFs by different concentrations of VEGF after a time-interval of 50 minutes. Similarly, Fig. 6(D) shows the time-dependent release profile of DOX in the presence of VEGF, 2 μM, curve (i) and in the absence of VEGF, curve (ii). After *ca.* 50 minutes, the release rate of DOX reached saturation, and using an appropriate calibration curve, the loading of DOX in the tetrahedra-gated NMOFs was derived and it corresponded to 71 nmols per mg of NMOFs. Fig. 6(E) shows the fluorescence spectra of the released DOX after unlocking the NMOFs by 2 μM of VEGF at different time-intervals. In addition, we note that the released VEGF-aptamer complex exhibits a G-quadruplex structure. This feature was confirmed by subjecting the released VEGF/tetrahedra structures to hemin to yield the respective catalytic hemin/G-quadruplex DNAzyme. The DNAzyme characteristic catalyzed oxidation of Amplex-Red to the fluorescent Resorufin was demonstrated, for details see ESI Fig. S7.† As before, a reference duplex (2)/(2″)-gated NMOFs carrying the load was prepared. For further characterization of the reference (2)/(2″) duplex-gated Rh 6G-loaded NMOFs see ESI, Fig. S8.† It should be noted that the tetrahedra-gated NMOFs and the (2)/(2″) duplex-gated NMOFs reveal similar loading degrees of the Rh 6G dye and DOX, similar coverages of the NMOFs by the tetrahedra and (2)/(2″) coatings, and similar sizes of the NMOFs.

The cell permeation efficacy and cytotoxicity of the VEGF-responsive tetrahedra-gated DOX-loaded NMOFs were examined toward MDA-MB-231 breast cancer cells and epithelial MCF-10A control breast cells, and compared to the reference (2)/(2″) duplex-gated NMOFs. Fig. 7(A) panel I and II show the confocal fluorescence microscopy images corresponding to the MDA-MB-231 cells treated with the DOX-loaded VEGF-responsive tetrahedra-gated or the (2)/(2″)-gated NMOFs, respectively, while panel III and IV show the fluorescence confocal microscopy images of the MCF-10A treated with the two types of DOX-loaded NMOFs, respectively. Fig. 7(B) shows the integrated fluorescence intensities normalized to the number of cells corresponding to the images of the gated systems described in Fig. 7(A) panels I to IV, in the form of a "bar" presentation (the error bars are derived by measuring $N = 10$ scanned areas of each of the systems). The fluorescence intensity of the VEGF-responsive DNA tetrahedra-gated NMOF penetrating the MDA-MB-231 cells is *ca.* 3-fold higher as compared to the permeation resulting upon uptake by the (2)/(2″)-gated NMOFs. The fluorescence generated by the permeation of the respective NMOFs into the MCF-10A cells is very low. That is the permeation of the DOX-loaded NMOFs into the MDA-MB-231 cancer cell is significantly higher as compared to the epithelial MCF-10A cells, and a superior permeation of the tetrahedra-gated DOX-loaded NMOFs into the cancer cells is observed, as compared to the reference (2)/(2″)-gated NMOFs.

The VEGF-induced release of DOX from the NMOFs, and the resulting cytotoxicity of the released drug towards the cancer cells are schematically presented in Fig. 7(C). Fig. 7(D) depicts the results corresponding to the cytotoxicity of the DOX-loaded

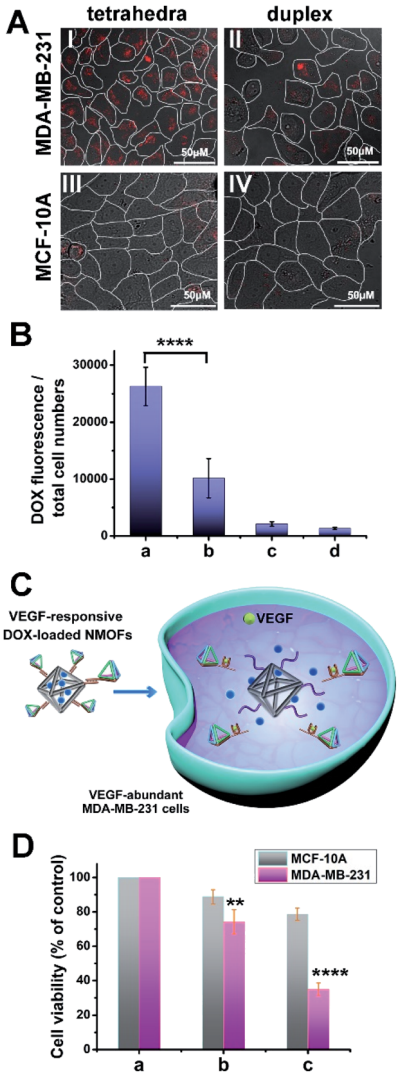

Fig. 7 (A) Fluorescence confocal microscopy images corresponding to: panel I-Uptake of the DOX-loaded VEGF-responsive tetrahedra-gated NMOFs by the MDA-MB-231 cells. Panel II-Uptake of the DOX-loaded VEGF-responsive (2)/(2″) duplex-gated NMOFs by the MDA-MB-231 cells. Panel III-Uptake of the DOX-loaded VEGF-responsive tetrahedra-gated NMOFs by the MCF-10A cells. Panel IV-Uptake of the DOX-loaded VEGF-responsive (2)/(2″) duplex-gated NMOFs by the MCF-10A cells. Cells treated with 60 μg mL^{-1} NMOFs for 6 hours. (B) Normalized integrated fluorescence intensities corresponding to the uptake of: (a) DOX-loaded VEGF-responsive tetrahedra-gated NMOFs treated MDA-MB-231 cells. (b) DOX-loaded VEGF-responsive (2)/(2″) duplex-gated NMOFs treated MDA-MB-231 cells. (c) DOX-loaded VEGF-responsive tetrahedra-gated NMOFs treated MCF-10A cells. (d) DOX-loaded VEGF-responsive (2)/(2″) duplex-gated NMOFs treated MCF-10A cells. Uptake of the different NMOFs by cells is measured in more than 80 cells per field (±SD, from 10 fields). (C) Schematic VEGF-triggered unlocking of NMOFs and release of DOX process with DOX-loaded VEGF-responsive tetrahedra-gated NMOFs into MDA-MB-231 cells. (D) Cytotoxicity of the DOX-loaded VEGF-responsive tetrahedra-gated NMOFs towards MDA-MB-231 cells (pink) and MCF-10A cells (grey) and the comparison to the cytotoxicity of the DOX-loaded VEGF-responsive (2)/(2″) duplex-gated NMOFs towards these cells: (a) untreated cells. (b) Cells treated with DOX-loaded VEGF-responsive (2)/(2″) duplex-gated NMOFs. (c) Cells treated with DOX-loaded VEGF-responsive tetrahedra-gated NMOFs. In all experiments, cells were treated with 60 μg mL^{-1} NMOFs for 6 hours and evaluating cell viability after three days and the NMOFs included DOX-loading corresponding to 71 nmols per mg of NMOFs. Error bars derived from $N = 3$ experiments. ** denotes $P < 0.01$, **** denotes $P < 0.0001$ by *t*-test.

VEGF-responsive tetrahedra-gated NMOFs towards the MDA-MB-231 breast cancer cells and the epithelial MCF-10A cells. For comparison, the cell viability of non-treated cells is shown in Fig. 7(D), panel a. Upon treatment of the cells with NMOFs, 60 μg mL^{-1}, subsequent washing the treated cells and examination of the cell viability after three days, a 65% MDA-MB-231 cell death is observed while only 20% cell death of the MCF-10A is observed, panel c. Under these conditions, the MDA-MB-231 cancer cells and MCF-10A cells are treated with the DOX-loaded (2)/(2″) duplex-gated NMOFs revealed cell mortalities corresponding to 25% and 10%, respectively, panel b. That is, the drug-loaded tetrahedra-gated NMOFs revealed significantly enhanced cytotoxic activities as compared to the reference DOX-loaded (2)/(2″) duplex-gated NMOFs. This result is consistent with the increased permeation efficacy of the DOX-loaded tetrahedra-gated NMOFs, as compared to the DOX-loaded (2)/(2″) duplex-gated NMOFs.

Beyond the application of the drug-loaded VEGF-responsive DNA tetrahedra-functionalized NMOFs as superior carriers for the chemotherapeutic treatment of cancer cells, we attempted to apply the superior aptamer-modified DNA tetrahedra cell permeation efficacy for enhanced photodynamic therapy (PDT) treatment of malignant cells. The VEGF-triggered unlocking of the tetrahedra-gated NMOFs yields a VEGF-aptamer G-quadruplex unit. Realizing, however, that Zn(II)-porphyrin, Zn(II)-PPIX, bound to G-quadruplex structures reveal superior photophysical enhanced fluorescence properties,[45] we argued that the design of VEGF-responsive aptamer-modified tetrahedra-functionalized NMOFs loaded with Zn(II)-PPIX photosensitizer units could be ideal carriers for PDT of cancer cells. The fluorescence intensity of the Zn(II)-PPIX associated with the G-quadruplex tetrahedra structure is *ca.* 8-fold higher as compared to the free Zn(II)-PPIX, see ESI† and accompanying discussion, Fig. S9.† The design of these carriers and their potential use as PDT agents is schematically introduced in Fig. 8(A). The (2)-functionalized NMOFs are loaded with the Zn(II)-PPIX photosensitizer and locked with (2′)-tethered DNA tetrahedra units to yield the Zn(II)-PPIX-loaded VEGF-responsive tetrahedra-gated NMOFs. Realizing the size of Zn(II)-PPIX, *ca.* 12 Å × 15 Å, we suggest that the photosensitizer load accommodates inter-pore domains of the porous NMOFs. In the presence of VEGF and K^+-ions, the tetrahedra are displaced while forming the VEGF-aptamer G-quadruplex-functionalized tetrahedra, and the concomitant release of Zn(II)-PPIX. The binding of Zn(II)-PPIX to the G-quadruplex nanostructures yields the active photosensitizer for the light-induced formation of the toxic reactive oxygen species, ROS. The effective selective permeation of the Zn(II)-PPIX-loaded tetrahedra-functionalized NMOFs into cancer cells is, then, anticipated to allow effective PDT treatment of malignant cells. For evaluation of the advantages of Zn(II)-PPIX-loaded tetrahedra-gated NMOFs, the Zn(II)-PPIX-loaded (2)/(2″) duplex-gated NMOFs were applied as a reference system. Fig. S10† shows the schematic structure of Zn(II) PPIX-loaded (2)/(2″) duplex-gated NMOFs. These NMOFs are anticipated to allow the VEGF-triggered release and formation of the Zn(II)-PPIX-bound VEGF-aptamer G-quadruplex units, yet the lower permeation efficacy of the reference NMOFs into cancer cells should emphasize the superior functions of the tetrahedra-modified carriers as PDT agents. To develop the Zn(II)-PPIX-loaded tetrahedra-functionalized NMOFs, the *in vitro* formation of the Zn(II)-PPIX G-quadruplex nanostructures upon the VEGF-triggered release of Zn(II)-PPIX should be supported, and the *in vitro* activity of the resulting Zn(II)-PPIX/VEGF-aptamer tetrahedra G-quadruplex should be

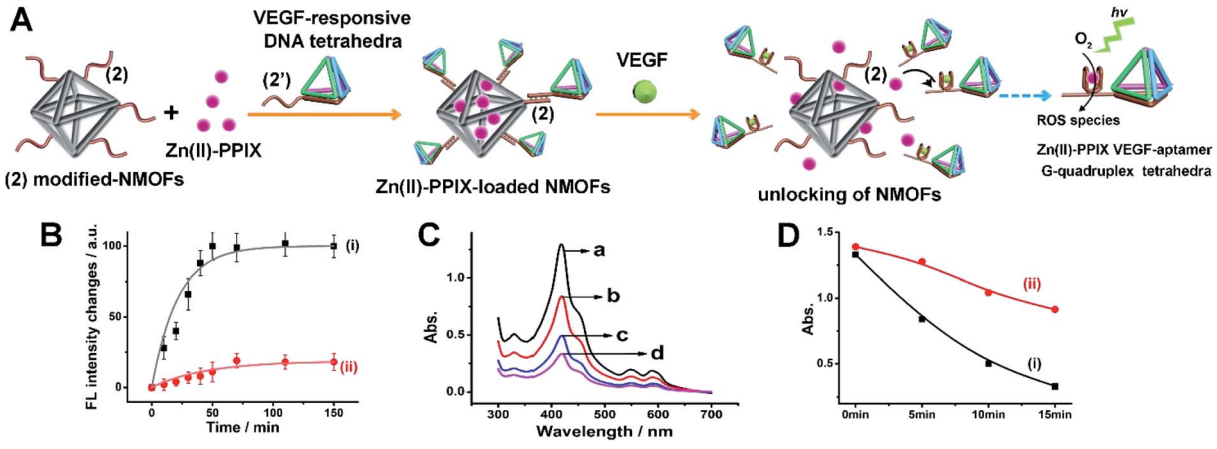

Fig. 8 (A) Preparation of Zn(II)-PPIX-loaded VEGF-responsive tetrahedra-gated NMOFs and the schematic VEGF-induced unlocking of the NMOFs and the photochemical generation of ROS by the resulting VEGF-aptamer G-quadruplex associated with the DNA tetrahedra. (B) Time-dependent release and formation of the Zn(II)-PPIX/VEGF aptamer linked to the tetrahedra: (i) in the presence of VEGF, 2 μM, (ii) in the absence of VEGF. (C) Absorbance spectra of the ROS agent detection probe, DPBF, upon photochemical releasing of the Zn(II)-PPIX-G-quadruplex tetrahedra from 0.1 mg loaded NMOFs, in the presence of K^+-ions, for a fixed time-interval of three hours and allowing the photoactivation of the ROS for different time-intervals: (a) 0 minutes; (b) 5 minutes; (c) 10 minutes and (d) 15 minutes. (D) Time-dependent absorbance changes of DPBF upon photochemical releasing of the Zn(II)-PPIX-G-quadruplex tetrahedra from 0.1 mg loaded NMOFs, for a fixed time-interval of three hours and allowing the photoactivation of the ROS for different time-intervals: (i) with K^+-ions; (ii) no K^+-ions. Error bars derived from $N = 3$ experiments.

demonstrated. Fig. 8(B) depicts the time-dependent VEGF-triggered release of the Zn(II)-PPIX from the tetrahedra-modified NMOFs. The formation of the Zn(II)-PPIX VEGF-aptamer G-quadruplex was supported by: (i) in the presence of added 18-crown-6-ether to the release mixture, the fluorescence intensities of the released Zn(II)-PPIX are substantially lower, Fig. S11,† since the included K^+-ions stabilizing the G-quadruplex are eliminated by the 18-crown-6-ether. (ii) Using an appropriate calibration curve of Zn(II)-PPIX/G-quadruplex, we estimated the loading and released content of Zn(II)-PPIX associated with the NMOFs to be 82 nmols per mg of NMOFs, Fig. S12.† The *in vitro* VEGF-triggered formation of ROS intermediates by the Zn(II)-PPIX-loaded DNA tetrahedra-functionalized NMOFs is demonstrated in Fig. 8(C). The probe, 1,3-diphenylisobenzofuran (DPBF), was used to follow the formation of ROS (*e.g.* $^1O_2$).[44] Fig. 8(C) depicts the spectral absorbance features of the ROS detection probe, upon subjecting the solution of the probe to the Zn(II)-PPIX-loaded VEGF-responsive tetrahedra-gated NMOFs for different time-intervals of illumination. As the illumination of the probe solution is prolonged, the depletion of the probe spectra are intensified, confirming that higher contents of ROS are formed as the illumination of the sample is prolonged. To support the enhanced efficacy of generation of the ROS products by the Zn(II)-PPIX/G-quadruplex tetrahedra structures, we compared the ROS generation efficiency by the Zn(II)-PPIX/K^+-ions-stabilized G-quadruplex tetrahedra to the ROS generated by Zn(II)-PPIX in the presence of the (2′)-modified tetrahedra, in the absence of K^+-ions (where the G-quadruplex is not formed), Fig. 8(D), curve (i) *vs.* (ii). We find a *ca.* 2.5-fold enhanced formation of the ROS products by the Zn(II)-PPIX/G-quadruplex tetrahedra.

The efficacy of PDT treatment of MDA-MB-231 breast cancer cells with the Zn(II)-PPIX-loaded VEGF-responsive DNA tetrahedra-gated NMOFs is presented in Fig. 9. In these experiments, the MDA-MB-231 breast cancer cells and MCF-10A epithelial breast cells were treated with the Zn(II)-PPIX-loaded tetrahedra-gated NMOFs and then were illuminated at λ = 405 nm, 30 mW cm^{-2} for a time-interval of 15 minutes and the cell viability was monitored after 3 days. The permeation features of the VEGF-responsive tetrahedra-gated NMOFs with the cancer cells, the VEGF-induced release of Zn(II)-PPIX from the NMOFs, and the resulting cytotoxicity by toxic ROS towards the cancer cells are schematically presented in Fig. 9(A). Control experiments included the PDT treatment of the MDA-MB-231 cells and MCF-10A cells with the reference NMOFs composed of Zn(II)-PPIX-loaded (2)/(2″) duplex-gated NMOFs under similar conditions. For comparison, the cell viability of non-treated cells is shown in Fig. 9(B), panel a. Further control experiments examined the effects of unloaded cells with illumination, panel b. The result reveals minute cell mortality (≤5%) upon illuminating the cells, demonstrating that illumination has no effect on cell death. The PDT treatment of the Zn(II)-PPIX-loaded (2)/(2″) duplex-gated NMOFs yields to 20% cell death of the MDA-MB-231 cancer cells while retaining 100% viability of the MCF-10A cells, panel c. More importantly is, however, the demonstration that the PDT of the MDA-MB-231 cells with the Zn(II)-PPIX-loaded tetrahedra-gated NMOFs led to *ca.* 70% cell death. While the MCF-10A were unaffected (100% viability), panel d. These results lead to important conclusions: (i) the Zn(II)-PPIX-loaded tetrahedra-gated NMOFs revealed a superior (4-fold) cytotoxic PDT treatment efficacy, as compared to the Zn(II)-PPIX-loaded (2)/(2″) duplex-gated NMOFs. (ii) The PDT treatment demonstrated selectivity towards the cancer cells as the epithelial MCF-10A cells were much less affected. These results are consistent with the fact that permeation into the MCF-10A cells is low. Furthermore, the low levels of VEGF in the epithelial cells prohibit the activation of the PDT by low levels of tetrahedra-gated NMOFs permeating into the MCF-10A cells.

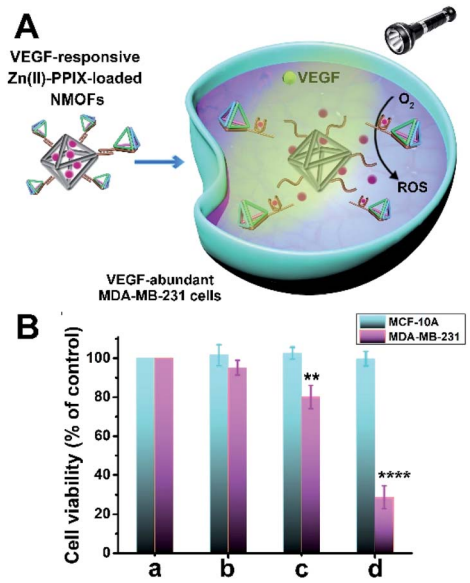

Fig. 9 (A) Schematic permeation of the Zn(II)-PPIX-loaded VEGF-responsive tetrahedra-gated NMOFs into MDA-MB-231 cancer cells (or MCF-10A epithelial breast cells) and the intracellular photodynamic generation of ROS that kill the cells. (B) Cytotoxicity of the PDT treatment of the respective cells treated with the Zn(II)-PPIX-loaded VEGF-responsive tetrahedra-gated NMOFs, and comparison of the results to the control systems where the cells are PDT treated with the Zn(II)-PPIX-loaded VEGF-responsive (2)/(2″) duplex-gated NMOFs: (a) untreated cells. (b) Cells unloaded with NMOFs, yet subject to light. (c) Cells treated to Zn(II)-PPIX-loaded VEGF-responsive (2)/(2″) duplex-gated NMOFs and subjected to PDT. (d) Cells treated to Zn(II)-PPIX-loaded VEGF-responsive tetrahedra-gated NMOFs and subjected to PDT. For all respective experiment, cells were treated with the NMOFs, 60 μg mL^{-1}, for six hours, and illuminated for 15 minutes, λ = 405 nm, 30 mW cm^{-2}, and cell viability was evaluated after three days. Error bars derived from $N = 3$ experiments. ** denotes $P < 0.01$, **** denotes $P < 0.0001$ by t-test.

Finally, it was essential to demonstrate the superior intracellular generation of the ROS products by the Zn(II)-PPIX-loaded DNA tetrahedra-gated NMOFs, as compared to (2)/(2″) duplex-gated NMOFs, in the MDA-MB-231 cancer cells, and the inefficient formation of the ROS agents in the MCF-10A cells. Fig. 10(A) shows the time-dependent confocal fluorescence images of, di(acetoxymethyl ester)-6-carboxy-2′,7′-dichlorodihydrofluorescein diacetate (CDCHF-DA), the ROS probe indicator generated in the respective cells by the Zn(II)-PPIX-loaded VEGF-aptamer G-quadruplex constituents released in the respective

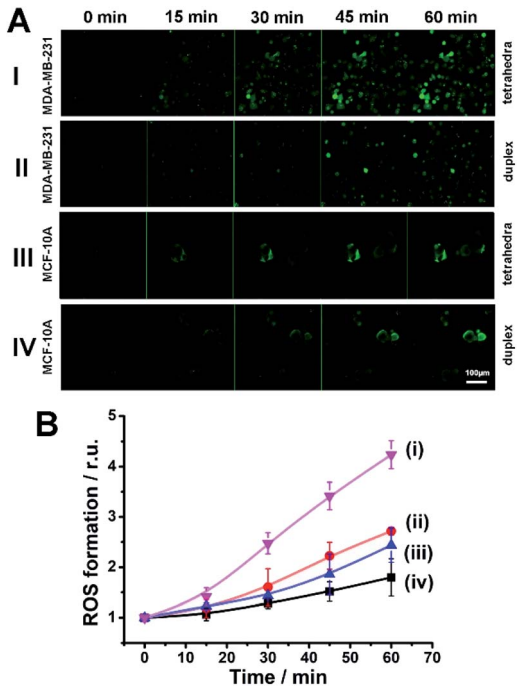

Fig. 10 (A) Panel I-Time-dependent confocal fluorescence images of ROS indicator in MDA-MB-231 cells treated with Zn(II)-PPIX-loaded VEGF-responsive tetrahedra-gated NMOFs. Panel II-Time-dependent confocal fluorescence images of ROS indicator in MDA-MB-231 cells treated with Zn(II)-PPIX-loaded VEGF-responsive (2)/(2″) duplex-gated NMOFs. Panel III-Time-dependent confocal fluorescence images of ROS indicator in MCF-10A cells treated with Zn(II)-PPIX-loaded VEGF-responsive tetrahedra-gated NMOFs. Panel IV-Time-dependent confocal fluorescence images of, CDCHF-DA, ROS indicator in MCF-10A cells treated with Zn(II)-PPIX-loaded VEGF-responsive (2)/(2″) duplex-gated NMOFs. Scale bars: 100 μm. (B) Normalized time-dependent fluorescence intensities of ROS indicator corresponding to: (i) MDA-MB-231 cells treated with Zn(II)-PPIX-loaded VEGF-responsive tetrahedra-gated NMOFs. (ii) MDA-MB-231 cells treated with Zn(II)-PPIX-loaded VEGF-responsive (2)/(2″) duplex-gated NMOFs. (iii) MCF-10A cells treated with Zn(II)-PPIX-loaded VEGF-responsive tetrahedra-gated NMOFs. (iv) MCF-10A cells treated with Zn(II)-PPIX-loaded VEGF-responsive (2)/(2″) duplex-gated NMOFs. For all respective experiment, cells were treated with the NMOFs, 60 μg mL^{-1}, for six hours, and illuminated for 15 minutes, $\lambda = 405$ nm, 30 mW cm^{-2}. Error bars derived from $N = 3$ experiments.

cell lines upon illumination at $\lambda = 405$ nm for a time-interval of 15 minutes (30 mW cm^{-2}). Fig. 10(B) shows the integrated time-dependent fluorescence intensities generated by the ROS probe. Clearly, most efficient fluorescence is generated by the VEGF-responsive tetrahedra-gated NMOFs in the MDA-MB-231 cancer cells, curve (i), and a significantly lower fluorescence is observed for the ROS probe generated by the VEGF-responsive (2)/(2″) duplex-gated NMOFs in these cells, curve (ii). Substantially lower ROS probe fluorescence intensities are observed for the MCF-10A cells functionalized with the respective gates. These results are consistent with the superior improved permeation of the Zn(II)-PPIX-loaded tetrahedra-gated NMOFs into the MDA-MB-231 cancer cells.

It should be noted that different drug-loaded carriers were unlocked in the presence of cellular biomarkers, such as ATP, miRNA or pH, to yield sense-and-treat therapeutic carriers.[46] The novelty of the present systems rests on the enhanced complexity of the carriers originating from the tethering of biomarker-responsive tetrahedra to the carrier that results in enhanced cell permeation and thus, improved sense-and-treat functions. In addition, the present study introduced the VEGF-aptamer-functionalized tetrahedra as gating units. Over-expressed VEGF in cancer cells was used, already, in the past, as biomarker to yield sense-and-treat carriers.[47] Nonetheless, in the present study, we utilize the fact that the unlocked VEGF-aptamer-modified tetrahedra consist of a G-quadruplex units that bind Zn(II)-PPIX to yield an effective PDT agent. Thus, the specific sense-and-treat system provides a carrier of dual functionalities that allow the unique release of a chemotherapeutic drug and the concomitant formation of a PDT agent.

Conclusions

The present study introduced aptamer-responsive DNA tetrahedra-gated metal organic framework nanoparticles, NMOFs, as functional carriers for biomedical applications. The NMOFs provide an effective carrier for drugs or PDT agents. The tetrahedra constituents gating the NMOFs introduces superior cell permeation nanostructures for efficient integration of the NMOFs carriers into cells. The bridging units linking the tetrahedra to the NMOFs provide the stimuli-responsive aptamer for unlocking the NMOFs and release of the loads *via* the formation of ligand–aptamer complexes. Two molecules that are abundant in cancer cells, *i.e.*, ATP or VEGF and their binding aptamers are used to unlock the drug (doxorubicin)-loaded carriers, resulting in effective selective cytotoxicity towards cancer cells. In addition, the VEGF-responsive aptamer-DNA tetrahedra-gated NMOFs loaded with the Zn(II)-PPIX photosensitizer is introduced. The VEGF-stimulated release of the Zn(II)-PPIX leads to the self-sustained assembly of the Zn(II)-PPIX/G-quadruplex units. VEGF-aptamer G-quadruplex-modified tetrahedra nanostructures act as an effective photodynamic therapy (PDT) agent for the generation of ROS. The effective tetrahedra-guided permeation of the PDT agents into cancer cells leads to selective and potent cytotoxicity towards cancer cells. The present study introduces important principles to design and tailor functional nanostructures for biomedical applications. By further engineering of the tetrahedra structures with specific aptamers recognizing cell receptors enhanced targeted specificity of cells is anticipated. In addition, the integration of other aptamers as stimuli-responsive elements, and the loading of the NMOFs with other drugs could lead to self-sustained functional nanostructures for treating other diseases.

Data availability

ESI that includes additional experimental details, sturcture of sequences, calibration curves related to the quantitive evaluaiton of the systems and release of loads from refenrece, duplex-gated NMOFs is provided.†

Author contributions

Pu Zhang and Amit Fischer performed the experiments. Yu Ouyang participated in the SEM, TEM and XRD experiments. Jianbang Wang performed the AFM and structural characterization of the tetrahedra. Yang Sung Sohn performed the fluorescence imaging and cell cytotoxicity studies. Rachel Nechushtai and Eli Pikarsky mentored the biological studies. Chunhai Fan consulted the experiments. Itamar Willner mentored the whole project. All authors participated in writing the manuscript and the evaluation of the results.

Conflicts of interest

There are no conflicts to declare.

Acknowledgements

This paper was supported by ISF-Precision Medicine Program grant no. 1696/20. The Shanghai Jiao Tong University, Shanghai, China-The Hebrew University cooperation program and the Minerva Center for Biohybrid Complex Systems.

Notes and references

1 (*a*) A. B. Cook and P. Decuzzi, *ACS Nano*, 2021, **15**, 2068–2098; (*b*) M. A. Hamburg and F. S. Collins, *N. Engl. J. Med.*, 2010, **363**, 301–304; (*c*) F. R. Vogenberg, C. I. Barash and M. J. P. Pursel, *Therapeutics*, 2010, **35**, 560.

2 (*a*) M. S. Alai, W. J. Lin and S. S. Pingale, *J. Food Drug Anal.*, 2015, **23**, 351–358; (*b*) V. Ravaine, C. Ancla and B. Catargi, *J. Controlled Release*, 2008, **132**, 2–11; (*c*) Q. Wu, L. Wang, H. Yu, J. Wang and Z. Chen, *Chem. Rev.*, 2011, **111**, 7855–7875.

3 (*a*) D. Shiino, Y. Murata, A. Kubo, Y. J. Kim, K. Kataoka, Y. Koyama, A. Kikuchi, M. Yokoyama, Y. Sakurai and T. J. Okano, *J. Controlled Release*, 1995, **37**, 269–276; (*b*) R. A. Siegel, Y. Gu, A. Baldi and B. Ziaie, *Macromol. Symp.*, 2004, **207**, 249–256; (*c*) W. Wu, N. Mitra, E. C. Yan and S. Zhou, *ACS Nano*, 2010, **4**, 4831–4839.

4 A. Fischer, S. Lilienthal, M. Vazquez-Gonzalez, M. Fadeev, Y. S. Sohn, R. Nechushtai and I. Willner, *J. Am. Chem. Soc.*, 2020, **142**, 4223–4234.

5 (*a*) W. H. Chen, G. F. Luo, M. Vazquez-Gonzalez, R. Cazelles, Y. S. Sohn, R. Nechushtai, Y. Mandel and I. Willner, *ACS Nano*, 2018, **12**, 7538–7545; (*b*) Y. Zhao, B. G. Trewyn, I. I. Slowing and V. S. Lin, *J. Am. Chem. Soc.*, 2009, **131**, 8398–8400.

6 P. Zhang, L. Yue, M. Vazquez-Gonzalez, Z. Zhou, W. H. Chen, Y. S. Sohn, R. Nechushtai and I. Willner, *ACS Nano*, 2020, **14**, 1482–1491.

7 W.-C. Liao, Y. S. Sohn, M. Riutin, A. Cecconello, W. J. Parak, R. Nechushtai and I. Willner, *Adv. Funct. Mater.*, 2016, **26**, 4262–4273.

8 (*a*) N. Ferrara, H.-P. Gerber and J. LeCouter, *Nat. Med.*, 2003, **9**, 669–676; (*b*) N. Ferrara, *Nat. Rev. Cancer*, 2002, **2**, 795–803; (*c*) A. Hoeben, B. Landuyt, M. S. Highley, H. Wildiers, A. T. Van Oosterom and E. A. De Bruijn, *Pharmacol. Rev.*, 2004, **56**, 549–580.

9 (*a*) P. Carmeliet and R. K. Jain, *Nature*, 2000, **407**, 249–257; (*b*) P. Salven, A. Orpana and H. Joensuu, *Clin. Cancer Res.*, 1999, **5**, 487–491; (*c*) P. Salven, V. Perhoniemi, H. Tykkä, H. Mäenpää and H. Joensuu, *Breast Cancer Res. Treat.*, 1999, **53**, 161–166.

10 H. Nakahara, J. Song, M. Sugimoto, K. Hagihara, T. Kishimoto, K. Yoshizaki and N. Nishimoto, *Arthritis Rheum.*, 2003, **48**, 1521–1529.

11 D. Ray, M. Mishra, S. Ralph, I. Read, R. Davies and P. J. D. Brenchley, *Diabetes*, 2004, **53**, 861–864.

12 M. Detmar, *J. Invest. Dermatol.*, 2004, **122**, xiv–xv.

13 E. Storkebaum, D. Lambrechts and P. Carmeliet, *Bioessays*, 2004, **26**, 943–954.

14 F. Ghavamipour, H. Rahmani, M. Shanehsaz, K. Khajeh, M. Mirshahi and R. H. Sajedi, *J. Nanobiotechnol.*, 2020, **18**, 93.

15 (*a*) A. Ravalli, L. Rivas, A. De la Escosura-Muniz, J. Pons, A. Merkoci and G. Marrazza, *J. Nanosci. Nanotechnol.*, 2015, **15**, 3411–3416; (*b*) M. Shamsipur, L. Farzin, M. Amouzadeh Tabrizi and F. Molaabasi, *Biosens. Bioelectron.*, 2015, **74**, 369–375.

16 R. Freeman, J. Girsh, A. F. Jou, J. A. Ho, T. Hug, J. Dernedde and I. Willner, *Anal. Chem.*, 2012, **84**, 6192–6198.

17 Z. Zhou, Y. S. Sohn, R. Nechushtai and I. Willner, *ACS Nano*, 2020, **14**, 9021–9031.

18 (*a*) P. Horcajada, R. Gref, T. Baati, P. K. Allan, G. Maurin, P. Couvreur, G. Ferey, R. E. Morris and C. Serre, *Chem. Rev.*, 2012, **112**, 1232–1268; (*b*) J. R. Li, J. Sculley and H. C. Zhou, *Chem. Rev.*, 2012, **112**, 869–932; (*c*) M. O'Keeffe and O. M. Yaghi, *Chem. Rev.*, 2012, **112**, 675–702; (*d*) C. Wang, T. Zhang and W. Lin, *Chem. Rev.*, 2012, **112**, 1084–1104; (*e*) O. M. Yaghi, M. O'Keeffe, N. W. Ockwig, H. K. Chae, M. Eddaoudi and J. Kim, *Nature*, 2003, **423**, 705–714.

19 P. Ling, J. Lei, L. Zhang and H. Ju, *Anal. Chem.*, 2015, **87**, 3957–3963.

20 B. Ghalei, K. Sakurai, Y. Kinoshita, K. Wakimoto, A. P. Isfahani, Q. Song, K. Doitomi, S. Furukawa, H. Hirao, H. Kusuda, S. Kitagawa and E. Sivaniah, *Nat. Energy*, 2017, **2**, 1–9.

21 H. B. Wu and X. W. D. Lou, *Sci. Adv.*, 2017, **3**, eaap9252.

22 (*a*) Y. Li, J. Tang, L. He, Y. Liu, Y. Liu, C. Chen and Z. Tang, *Adv. Mater.*, 2015, **27**, 4075–4080; (*b*) K. M. Taylor-Pashow, J. Della Rocca, Z. Xie, S. Tran and W. Lin, *J. Am. Chem. Soc.*, 2009, **131**, 14261–14263.

23 (*a*) W. Cai, J. Wang, C. Chu, W. Chen, C. Wu and G. Liu, *Adv. Sci.*, 2019, **6**, 1801526; (*b*) Z. Dong, Y. Sun, J. Chu, X. Zhang and H. Deng, *J. Am. Chem. Soc.*, 2017, **139**, 14209–14216; (*c*) K. Lu, T. Aung, N. Guo, R. Weichselbaum and W. Lin, *Adv. Mater.*, 2018, **30**, e1707634; (*d*) Y. Wang, J. Yan, N. Wen, H. Xiong, S. Cai, Q. He, Y. Hu, D. Peng, Z. Liu and Y. Liu, *Biomaterials*, 2020, **230**, 119619.

24 Z. Zhou, M. Vazquez-Gonzalez and I. Willner, *Chem. Soc. Rev.*, 2021, **50**, 4541–4563.

25 (*a*) Z. Shi, X. Chen, L. Zhang, S. Ding, X. Wang, Q. Lei and W. Fang, *Biomater. Sci.*, 2018, **6**, 2582–2590; (*b*) L. L. Tan, H. Li, Y. C. Qiu, D. X. Chen, X. Wang, R. Y. Pan, Y. Wang, S. X. Zhang, B. Wang and Y. W. Yang, *Chem. Sci.*, 2015, **6**, 1640–1644.

26 B. Lei, M. Wang, Z. Jiang, W. Qi, R. Su and Z. He, *ACS Appl. Mater. Interfaces*, 2018, **10**, 16698–16706.

27 S. Wang, Y. Chen, S. Wang, P. Li, C. A. Mirkin and O. K. Farha, *J. Am. Chem. Soc.*, 2019, **141**, 2215–2219.

28 J. S. Kahn, L. Freage, N. Enkin, M. A. Garcia and I. Willner, *Adv. Mater.*, 2017, **29**, 1602782.

29 (*a*) W. H. Chen, X. Yu, A. Cecconello, Y. S. Sohn, R. Nechushtai and I. Willner, *Chem. Sci.*, 2017, **8**, 5769–5780; (*b*) W.-H. Chen, G.-F. Luo, Y. S. Sohn, R. Nechushtai and I. Willner, *Adv. Funct. Mater.*, 2019, **29**, 1805341.

30 W. H. Chen, G. F. Luo, Y. S. Sohn, R. Nechushtai and I. Willner, *Small*, 2019, **15**, e1900935.

31 W. H. Chen, S. Yang Sung, M. Fadeev, A. Cecconello, R. Nechushtai and I. Willner, *Nanoscale*, 2018, **10**, 4650–4657.

32 Q. Hu, H. Li, L. Wang, H. Gu and C. Fan, *Chem. Rev.*, 2019, **119**, 6459–6506.

33 (*a*) R. P. Goodman, M. Heilemann, S. Doose, C. M. Erben, A. N. Kapanidis and A. J. Turberfield, *Nat. Nanotechnol.*, 2008, **3**, 93–96; (*b*) T. R. Wilks, J. Bath, J. W. de Vries, J. E. Raymond, A. Herrmann, A. J. Turberfield and R. K. O'Reilly, *ACS Nano*, 2013, **7**, 8561–8572; (*c*) D. Zhu, H. Pei, G. Yao, L. Wang, S. Su, J. Chao, L. Wang, A. Aldalbahi, S. Song, J. Shi, J. Hu, C. Fan and X. Zuo, *Adv. Mater.*, 2016, **28**, 6860–6865.

34 (*a*) Z. Ge, M. Lin, P. Wang, H. Pei, J. Yan, J. Shi, Q. Huang, D. He, C. Fan and X. Zuo, *Anal. Chem.*, 2014, **86**, 2124–2130; (*b*) H. Pei, N. Lu, Y. Wen, S. Song, Y. Liu, H. Yan and C. Fan, *Adv. Mater.*, 2010, **22**, 4754–4758.

35 H. Pei, L. Liang, G. Yao, J. Li, Q. Huang and C. Fan, *Angew. Chem., Int. Ed. Engl.*, 2012, **51**, 9020–9024.

36 Z. Zhou, P. Zhang, L. Yue and I. Willner, *Nano Lett.*, 2019, **19**, 7540–7547.

37 A. J. Mastroianni, S. A. Claridge and A. P. Alivisatos, *J. Am. Chem. Soc.*, 2009, **131**, 8455–8459.

38 M. Li, H. Ding, M. Lin, F. Yin, L. Song, X. Mao, F. Li, Z. Ge, L. Wang, X. Zuo, Y. Ma and C. Fan, *J. Am. Chem. Soc.*, 2019, **141**, 18910–18915.

39 (*a*) J. Li, H. Pei, B. Zhu, L. Liang, M. Wei, Y. He, N. Chen, D. Li, Q. Huang and C. Fan, *ACS Nano*, 2011, **5**, 8783–8789; (*b*) W. Ma, Y. Zhan, Y. Zhang, X. Shao, X. Xie, C. Mao, W. Cui, Q. Li, J. Shi, J. Li, C. Fan and Y. Lin, *Nano Lett.*, 2019, **19**, 4505–4517; (*c*) A. S. Walsh, H. Yin, C. M. Erben, M. J. Wood and A. J. Turberfield, *ACS Nano*, 2011, **5**, 5427–5432.

40 P. Peng, Y. Du, J. Zheng, H. Wang and T. Li, *Angew. Chem., Int. Ed. Engl.*, 2019, **58**, 1648–1653.

41 (*a*) Z. Liu, H. Pei, L. Zhang and Y. Tian, *ACS Nano*, 2018, **12**, 12357–12368; (*b*) Z. Qing, J. Hu, J. Xu, Z. Zou, Y. Lei, T. Qing and R. Yang, *Chem. Sci.*, 2020, **11**, 1985–1990; (*c*) J. Su, F. Wu, H. Xia, Y. Wu and S. Liu, *Chem. Sci.*, 2020, **11**, 80–86; (*d*) J. Wang, D. X. Wang, J. Y. Ma, Y. X. Wang and D. M. Kong, *Chem. Sci.*, 2019, **10**, 9758–9767.

42 I. A. Lázaro, S. Haddad, S. Sacca, C. Orellana-Tavra, D. Fairen-Jimenez and R. S. Forgan, *Chem*, 2017, **2**, 561–578.

43 R. Mo, T. Jiang, R. DiSanto, W. Tai and Z. Gu, *Nat. Commun.*, 2014, **5**, 1–10.

44 K. Lu, C. He and W. B. Lin, *J. Am. Chem. Soc.*, 2015, **137**, 7600.

45 Z. Zhang, E. Sharon, R. Freeman, X. Liu and I. Willner, *Anal. Chem.*, 2012, **84**, 4789.

46 (*a*) P. Zhang, C. Wang, J. Zhao, A. Zhao, Q. Shen, L. Li, J. Li, J. Zhang, Q. Min, J. Chen, H.-Y. Chen and J.-J. Zhu, *ACS Nano*, 2016, **10**, 3637–3647; (*b*) Z. Zhang, D. Balogh, F. Wang and I. Willner, *J. Am. Chem. Soc.*, 2013, **135**, 1934–1940; (*c*) L. Zhang, H. Qin, J. Li, J.-N. Qiu, J.-M. Huang, M.-C. Li and Y.-Q. Guan, *J. Mater. Chem. B*, 2018, **6**, 745107461; (*d*) Y. Zhao, Z. Luo, M. Li, Q. Qu, X. Ma, S.-H. Yu and Y. Zhao, *Angew. Chem., Int. Ed. Engl.*, 2015, **54**, 919–922; (*e*) P. Zhang, F. Cheng, R. Zhou, J. Cao, J. Li, C. Burda, Q. Min and J.-J. Zhu, *Angew. Chem.*, 2014, **126**, 2403–2407.

47 R. Freeman, J. Girsh, A. Fang-ju, J. A. A. Ho, T. Hug, J. Dernedde and I. Willner, *Anal. Chem.*, 2012, **84**, 6192–6198.